

Origin of broad He II 4686 Å emission in early spectra of type IIP supernovae

© 2024 N. N. Chugai¹ and V. P. Utrobin^{2,1}

¹ *Institute of astronomy, Russian Academy of Sciences, Moscow*

² *SRC “Kurchatov institute”, Moscow*

Submitted 05.10.2023

Keywords: stars – supernovae; stars – stellar wind

PACS codes:

arXiv:2402.18299v1 [astro-ph.HE] 28 Feb 2024

¹email: nchugai@inasan.ru

Abstract

We propose a model for the origin of the broad He II 4686 Å emission in the early spectrum of type II SN 2020jfo. The 4686 Å line is emitted presumably by dense fragments embedded into a hot gas of the forward shock wave. The fragments are produced as a result of a heavy braking of the dense low-mass shell at the ejecta boundary and a simultaneous Rayleigh-Taylor instability. The temperature of line-emitting fragments is $\approx 5 \times 10^4$ K. Calculations of ionization and excitation of helium and hydrogen account for the He II 4686 Å luminosity, the large flux ratio of He II 4686 Å/H α , and a significant optical depth of the 4686 Å line. We demonstrate that fragments heating by hot electrons behind the forward shock compensates cooling via the He II 304 Å emission.

1 INTRODUCTION

Supernovae (SNe) of types IIP and IIL are the result of a core collapse of a massive red supergiant (RSG). In some cases early spectra show signature of more vigorous mass loss by a presupernova (pre-SN) compared to ordinary RSG (Chugai 2001; Groh 2014; Yaron et al. 2017). The density of the circumstellar (CS) matter in a close vicinity is a crucial factor that can affect the SN bolometric luminosity and this effect should be taken into account in the hydrodynamic modelling (Blinnikov & Bartunov 1993; Chugai 2001; Morozova et al. 2017).

Despite a high degree of development and verification of applied methods of the radiation hydrodynamics, the SN parameters (explosion energy, ejecta mass and pre-SN radius) recovered by different authors can differ by a factor of 1.5 – 2 due to a different choice of the CS gas density. This situation is illustrated by type IIP SN 2020jfo: the CS shell mass within the radius of 10^{15} cm is $0.2 M_{\odot}$ in the model by Teja et al. (2022) compared to $\sim 10^{-3} M_{\odot}$ in the alternative model (Utrobín & Chugai 2024). In the first case the large CS mass is obtained based on the description of the early stage of the light curve, whereas in the second case the mass of the CS shell is the result of both the hydrodynamic modelling and making use of the spectral information, particularly, on the He II 4686 Å emission. The latter indicates the high expansion velocity, i.e., the negligible deceleration and therefore, the rarefied CS medium.

The He II 4686 Å emission is an essentially unique noticeable broad line in early spectrum, which permits us to directly estimate the expansion velocity of the outermost ejecta of SN IIP/L at the very early stage. Realizing a diagnostic value of this line, it is appropriate to pose a question, whether we understand the physical conditions in the line-emitting region adequately enough to rule out doubts on the boundary velocity recovered from this line.

The broad He II 4686 Å emission was observed during the initial several days after the explosion in other SNe IIP as well, including SN 2006bp

(Quimby et al. 2007), SN 2013fs (Bullivant et al. 2018), SN 2017gmr (Andrews et al. 2019), and SN 2023ixf (Jacobson-Galán et al. 2023). In each case the He II 4686 Å indicates large expansion velocity of the line-emitting gas and significant blueshift. Another important feature is a high flux ratio $f(4686)/f(\text{H}\alpha)$. For SN 2020jfo we estimate this ratio in the range of 4 – 5 based on the spectrum of Teja et al. (2022). This can be compared to the maximum ratio among planetary nebulae $f(4686)/f(\text{H}\alpha) \sim 0.2$ (Bohigas 2022).

There is no common opinion on the origin of the broad 4686 Å emission. A model proposed earlier for the 4686 Å line in SN 2013fs suggests that this line is emitted by dense fragments produced as a result of the deceleration of outer SN layers and a concomitant Rayleigh-Taylor (RT) instability (Chugai 2020). However, the issue of physical conditions in the line-emitting fragments was not discussed, except for the conclusion that the layer of fragments must be thin and adjoin the photosphere with sharp boundary. Besides, the dome-like profile shape suggests that fragments should be optically thick in the 4686 Å line frequencies.

Recently Shrestha et al. (2023) have compared the He II 4686 Å in the spectrum of SN 2023axu with the model r1w1 of early spectrum of SN IIP with a CS wind of $\dot{M} = 10^{-6}(u/10\text{km/s}) M_{\odot} \text{yr}^{-1}$ (Dessart et al. 2017). The model satisfactorily describes the 4686 Å profile at +1.1 d, but at later moment (+1.5 d) the agreement is broken: the model profile becomes symmetric in contrast to the blueshift and asymmetry of the observed profile. It should be emphasized that in the model r1w1 the adiabatic forward shock is absent despite the low wind density. The issue of the adequate model for the broad He II 4686 Å emission in early spectra of SNe IIP thus remains open.

Below we study conditions that account for the major properties of the broad He II 4686 Å emission in the spectrum of SN 2020jfo. We start with a general picture, then calculate the luminosities of the H α and 4686 Å lines, and recover conditions (mass of emitting fragments and kinetic temperature), which reproduce the major properties of the 4686 Å emission. Finally, we consider the issue of fragments heating by hot electrons of the forward shock, which should compensate the cooling via the He II 304 Å line.

2 CONDITIONS IN 4686 Å LINE-EMITTING ZONE

2.1 GENERAL PICTURE

According to the hydrodynamic model of SN 2020jfo, the shock breakout (SBO) occurs at 0.5 d after the explosion (Utrobin & Chugai 2024). Following the SBO, the SN ejecta generates a forward shock wave in the pre-SN wind that, for the moderate wind density, turns out adiabatic in contrast to the radiative reverse shock. However, at the very early stage the viscous velocity jump at the forward shock can be small compared to the boundary SN velocity because of the wind acceleration by the SN radiation. Let us

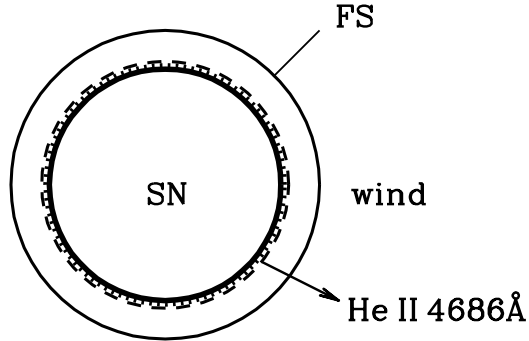


Figure 1. Schematic picture for the origin of the He II 4686 Å emission. Unperturbed SN envelope is bounded by the thin dense shell that serves as the photosphere (thick line circle). Right outside the photosphere lies the layer of dense fragments produced due to the RT instability brought about by the deceleration of outermost ejecta in the wind. Hot gas of the adiabatic forward shock maintains the high density and heating of fragments responsible for the He II 4686 Å emission.

estimate this effect.

In SN 2020jfo at $t = 2$ d the photosphere with the luminosity of $L \approx 3 \times 10^{42}$ erg s $^{-1}$ coincides with the thin shell at the SN boundary that expands with the speed of 16500 km s $^{-1}$. The SN radiation accelerates the preshock wind up to a velocity

$$v_{acc} \approx \frac{\kappa L}{4\pi v^2 ct} \approx 10^3 L_{43} / v_4^2 t_d \quad \text{km s}^{-1}, \quad (1)$$

where $\kappa = 0.34$ cm 2 g $^{-1}$ is the Thomson opacity, v is the SN boundary velocity, c is speed of light, L_{43} is the SN luminosity in 10^{43} erg s $^{-1}$, v_4 is the SN boundary velocity in 10^4 km s $^{-1}$, t_d is time in days. For $v_4 = 1.65$ and $t_d = 2$ the preshock wind velocity is about 200 km s $^{-1}$, almost two order lower the boundary SN speed. The contribution of a line opacity could increase this estimate by a factor less than two (Chugai et al. 2002).

We therefore conclude that the radiative acceleration of the preshock wind does not affect the viscous jump and the temperature at the forward shock. This conclusion is not relevant in the case of a massive optically thick CS shell around some SNe, when the forward shock due to a strong preshock heating by the radiation presursor (aka Marshak wave) propagates in the regime of the isothermal jump (Blinnikov 2008).

Noteworthy, after the SBO the formation of the adiabatic forward shock in the rarefied wind, $w = \dot{M}/u \lesssim 10^{15}$ g cm $^{-1}$, poses problems for the hydrodynamic modelling. This is related to the rapid transition from the optically thick to the optically thin regime of the shock wave propagation. Probably for this reason the SN IIP explosion and a subsequent formation of the adiabatic forward shock with the temperature of ~ 100 keV has not yet been implemented. The early formation of the adiabatic forward shock in SN IIP is evidenced by the hard X-rays ($T_x > 60$ keV) from SN 2023ixf on day 4

after the explosion (Grefenstette et al. 2023), despite the CS wind in this case is relatively dense, $w \sim 3 \times 10^{15} \text{ g cm}^{-1}$.

The broad He II 4686 Å emission is present in the spectrum of SN 2020jfo (Teja et al. 2022) on day 2.1 after the explosion (the adopted explosion date is MJD 58973.83) with the luminosity of $\approx 4 \times 10^{39} \text{ erg s}^{-1}$. According to the SN hydrodynamic model and the CS interaction model (Utrobin & Chugai 2024), at this moment the SN boundary velocity is 16500 km s^{-1} and the radius is $3.2 \times 10^{14} \text{ cm}$. The inferred wind parameter $w = \dot{M}/u = 2.2 \times 10^{15} \text{ g cm}^{-1}$ (u is the wind speed) suggests the baryon density $n_w = 10^9 \text{ cm}^{-3}$ at this radius.

The outer ejecta boundary serves as a spherical piston that drives the forward shock with the postshock temperature $T_s = (3/16)\mu m_p v_s^2/k = 4 \times 10^9 (v_s/17000 \text{ km/s})^2 \text{ K}$ and density $n_s = 4n_w$. The forward shock at the given moment is essentially adiabatic. Interestingly, the Compton cooling of hot electrons dominates over the bremsstrahlung radiation but this does not change conclusion on the adiabatic regime of the forward shock.

In the proposed picture the He II 4686 Å emission forms in the narrow layer right next to the photosphere that in turn coincides with the boundary ejecta dense shell (Fig. 1). The line-emitting layer is a two-phase medium in which the relatively cold dense fragments with temperature $T \lesssim 10^5 \text{ K}$ are embedded in the hot gas with temperature $T_s \approx 4 \times 10^9 \text{ K}$. The fragments are presumably produced as a result of the RT instability developed due to the deceleration of the outermost ejecta in the CS gas.

In the development of the RT instability of a decelerated dense shell one can distinguish three stages (cf. Blondin & Ellison 2001). At the first stage spikes of the cold dense shell penetrate the rarefied hot gas of the forward shock. At the second stage spikes are subject to the Kelvin-Helmholtz (KH) instability that generates a mushroom structure of spikes. This brings about the formation of thin layers of the cold dense gas with a large surface area. These dense layers are presumably responsible for the emergence of the He II 4686 Å emission. The third stage corresponds to a final fragmentation and a complete mixing of the dense cold gas with the hot gas of the forward shock. The fragments mixing is signaled by the disappearance of the broad He II 4686 Å emission.

The scenario based on the RT instability of the boundary dense shell has an important advantage compared to the conceivable origin of the He II 4686 Å emission from a stable thin dense shell, because it connects the duration of the He II 4686 Å emission (2–3 d) with a total time of the development of the RT instability until the complete mixing of cold fragments with the hot gas. This chain of events is inconsistent with the long-duration emission from the stable thin dense shell heated by the hard radiation or hot electrons of the forward shock.

The noted unusually high flux ratio $f(4686)/f(\text{H}\alpha) \sim 4 - 5$ in the SN 2020jfo spectrum indicates a dominant role of the collisional excitation of He II. This, in turn, suggests the kinetic temperature close to the temperature of the collisional ionization of He II, i.e. $5 \times 10^4 \text{ K}$. Hydrogen in this

Table. Model parameters.

Parameter	Value
Radius r [10^{14} cm]	3.2
Velocity v [10^9 cm/s]	1.65
Wind parameter w [10^{15} g cm $^{-1}$]	2.2
Mass of cold component M [M_{\odot}]	10^{-8}
Parameter of surface area ζ	2.5
Fragments surface density N_b [cm $^{-2}$]	3.7×10^{18}

case is strongly ionized and its emission is predominantly due to the recombination with a minor contribution of collisional excitation because of low fraction of neutrals. That presumably is the physics behind the large flux ratio He II 4686Å/H α .

2.2 IONIZATION, EXCITATION AND FRAGMENTS EMISSION

To confirm the outlined picture, we calculate ionization and excitation of He II and hydrogen for certain mass of fragments and kinetic temperature in the range of $10^4 - 10^6$ K. In the isobaric approximation the baryon number density in a fragment for a given temperature of cold gas T is equal $n = n_s T_s / T$. The emitting gas mass and density imply an emitting volume and a surface baryon density of fragments $N_b = M / 4\pi r^2 \zeta m_p$, where r is the radius of the boundary dense shell, and ζ is the parameter of the total surface area of fragments — one sided surface of flat fragments. The latter parameter, generally, might be found from 3D hydrodynamic modelling of the SN/CSM interaction and the concomitant RT instability. Yet the complexity of this approach is obvious even in the adiabatic case (Blondin & Ellison 2001).

The ionization fractions of hydrogen and helium for the normal abundances are calculated with the collisional ionization from two low levels and the radiative Case B recombination. A photoionization by the SN radiation is neglected. A population of the second level of hydrogen and He II is determined taking into account a multiple scattering of the resonant radiation and a local escape with the probability $\beta_{ik} = [1 - \exp(-\tau_{ik})] / \tau_{ik}$, where $\tau_{ik} = \sigma_0 f_{ik} \lambda_{ik} N_i / u_t$. Here σ_0 is the line integral cross section, f_{ik} is the oscillator strength, λ_{ik} is the wavelength, N_i is the column density of ion/atom on the lower level of a transition, u_t is the local velocity dispersion adopted to be equal the isothermal sound velocity.

The collisional ionization of hydrogen and helium is calculated using the classical ionization cross section averaged over the Maxwell distribution. The collisional excitation rates for He II are determined in the van Regemorter (1962) approximation, whereas for hydrogen we use the collisional rates from Vernazza et al. (1981). For hydrogen we take into account three lower levels

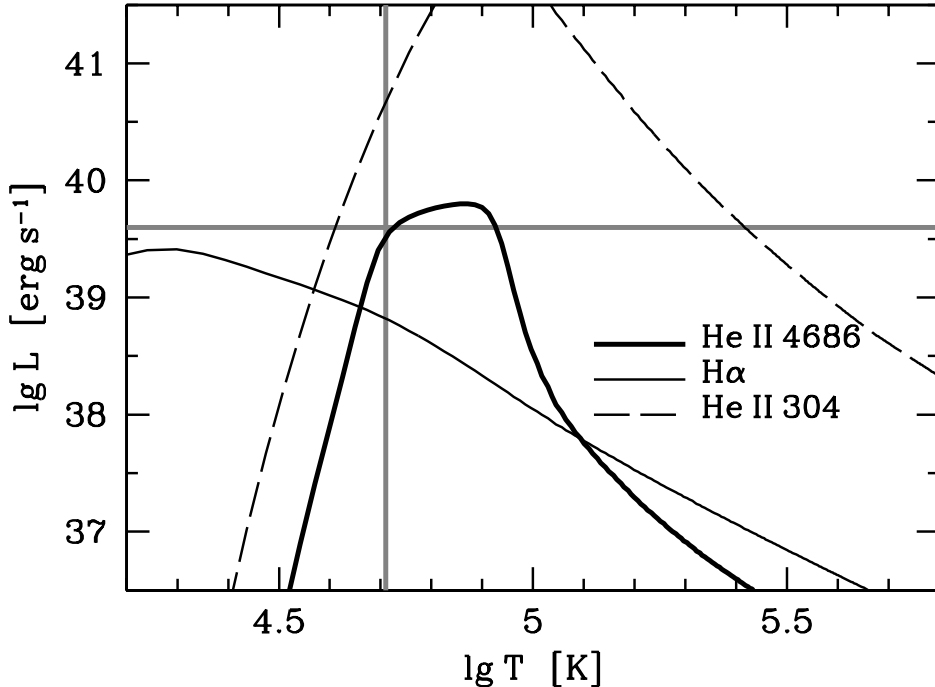


Figure 2. Model luminosity in lines of He II 4686 Å (*thick line*), H α (*thin line*) and He II 304 Å (*dashed line*) as a function of fragments temperature. *Horizontal line* shows the observational luminosity of He II 4686 Å, *vertical line* corresponds to the temperature fixed by the description of the He II 4686 Å luminosity, the ratio of He II 4686 Å/H α \sim 5 and assuming minimal luminosity of He II 304 Å.

plus continuum, whereas for He II four lower levels plus continuum are taken into account.

In the local escape approximation the line luminosity is determined by the total rate of the collisional excitation of the upper level of a certain transition C_k [$\text{cm}^{-3} \text{s}^{-1}$], by the rate of the local escape $A_{ki}\beta_{ik}$, and by the rate of the collisional transition to all lower levels D_k . The line luminosity is then $L_{ik} = C_k h\nu_{ik} V A_{ki}\beta_{ik} / (A_{ki}\beta_{ik} + D_k)$, where V is the total volume of the line-emitting fragments. Recombination emission rates for the H α and He II lines correspond to the Case B (Osterbrock & Ferland 2006).

2.3 RESULTS

The calculated luminosity vs. temperature for H α , He II 4686 Å, and He II 304 Å in SN 2020jfo at 2.1 d after the explosion is shown in Fig. 2. Input model parameters are listed in the first three lines of Table. Lower three lines of Table contain the mass of the emitting gas, the parameter ζ and the surface barion density determined by the total mass of fragments and their total surface area. The mass and ζ are inferred from the agreement between the calculated and observational luminosity of the 4686 Å line. The parameter ζ is responsible for the choice of the optimal fragment surface

density that secures an acceptable value of the photon escape probability.

The collisional excitation of He II results in the significant excess of the He II 4686 Å luminosity over that of H α in the temperature range of $(4.5 - 8) \times 10^4$ K thus confirming the above suggestion. Figure 2 displays also the He II 304 Å luminosity; this line dominates in radiative energy losses in the considered temperature range and therefore is crucial for the energy balance.

A key modelling result is the fixing of the optimal temperature $T \approx 52000$ K at which three major properties of the He II 4686 Å emission are reproduced, namely, the luminosity, the large flux ratio 4686 Å/H $\alpha \approx 5$, and the significant line optical depth $\tau_{34} \approx 5$. At this temperature the radiative energy losses are minimal with the He II 304 Å luminosity of 4×10^{40} erg s $^{-1}$.

3 FRAGMENTS HEATING

The X-ray luminosity of the forward shock amounts to 10^{41} erg s $^{-1}$ at the considered stage (Utrobín & Chugai 2024). However, given the high temperature of the bremsstrahlung radiation (~ 300 keV) and the low surface density of fragments ($\sim 10^{-4}$ g cm $^{-2}$), the power absorbed by fragments turns out mediocre $\lesssim 10^{37}$ erg s $^{-1}$, significantly smaller than the He II 304 Å luminosity.

An alternative mechanism is the electron thermal conductivity. Let us evaluate this possibility neglecting at the moment, the magnetic field. Given the low cross section of the fast electron scattering and the low surface density of fragments, the scattering probability with a significant energy transfer turns out small, $p \sim 10^{-3}$. Maximal velocities of hot electrons are subrelativistic ($\beta = v/c \sim 1$), so one needs to use the relativistic expression for the electron kinetic energy $E = mc^2(\gamma - 1)$, where $\gamma = 1/\sqrt{1 - \beta^2}$. This expression enters the Maxwell distribution $f(\beta) \propto \beta^2 \exp(-E(\beta)/kT)$ with $\beta < 1$.

Line-emitting fragments reside in the thin layer close to the contact surface SN ejecta/stellar wind ($R = 1$). According to self-similar solution (Chevalier 1982a; Nadyozhin 1985), for the wind density $\rho \propto 1/r^2$ and the SN density $\rho \propto 1/v^7$, at the fiducial radius $R = 1.05$ density is twice as high and temperature is twice as low as values at the shock front. We adopt conditions in the hot plasma at the radius $R = 1.05$ for the fragments environment. In this case the average energy of hot electrons in the flux toward certain direction is 164 keV, while the average speed of electrons is $\beta = 0.54$.

The energy loss by a fast electron in plasma per unit length (Breizman et al. 2019) is

$$\frac{dE}{ds} = -\frac{2\pi e^4 n_e}{mc^2 \beta^2} \ln \left[\frac{m^2 c^4 (\gamma^2 - 1)(\gamma - 1)}{2(\hbar\omega_p)^2 \gamma^2} \right], \quad (2)$$

where n_e is the electron number density in fragments, m is the electron mass, ω_p is the plasma frequency, while other notations are standard. The mean pass length of electron crossing flat fragment is $l = 2b \approx 2.5 \times 10^4$ cm, where $b = N_b/n_b \approx 1.25 \times 10^4$ cm is the average thickness of fragment. The average

energy lost by a fast electron during crossing fragment is $\Delta E = (dE/ds)l$, while the energy flux deposited in a fragment is $q = (1/4)y_e n_s c \beta \Delta E \approx 9.7 \times 10^9 \text{ erg s}^{-1} \text{ cm}^{-2}$, where $y_e = 0.85$ is the number of electrons per baryon, $n_s = 4 \times 10^9 \text{ cm}^{-3}$ is the number density of baryons at the shock front. The total heating power for all fragments is then $L_{inj} = 8\pi r^2 \zeta q \approx 6.2 \times 10^{40} \text{ erg s}^{-1}$ (heat flux through both sides is included). The estimated power, therefore, fully compensates the energy loss via the He II 304 Å emission ($4 \times 10^{40} \text{ erg s}^{-1}$).

The magnetic field that can be generated by turbulence related to the RT instability (Chevalier 1982b) unlikely inhibits the hot electrons penetration into fragments. The giroradius of a fast electron $r_e = \beta \gamma m c^2 / e B$ is equal to the fragment thickness $b \approx 1.2 \times 10^4 \text{ cm}$ for the magnetic field of $B \approx 0.3 \text{ G}$. This value is comparable to the field invoked for the interpretation of early radio emission of SNe IIP (Chevalier et al. 2006; Yadav et al. 2014). We therefore do not expect the magnetic field in SN 2020jfo substantially exceeding 0.3 G. Unexpectedly, the effect of such a field is boosting, and not inhibiting, the heating by electrons, since the electron pass curvature caused by the magnetic field increases the residence time of the fast electron in fragments.

4 DISCUSSION

The proposed model for the broad He II 4686 Å emission in the early spectrum of SN 2020jfo explains satisfactorily its major properties — large blueshift, the line luminosity, the large flux ratio He II 4686 Å/H α and the significant line optical depth. The model thus catches the basic physics involving the line-emitting dense fragments with the temperature of $\approx 5 \times 10^4 \text{ K}$ embedded in the hot gas of the forward shock. The proposed model is applicable to other SNe IIP with the broad He II 4686 Å emission in the early spectra. This model is an alternative with respect to the model of the early spectra of SNe IIP (Dessart et al. 2017) without the adiabatic forward shock, but showing the broad He II 4686 Å emission.

The line-emitting gas responsible for the broad 4686 Å emission in our model is related to the boundary thin dense shell that is liable to the RT instability. This boundary thin shell forms at the SBO stage of the exploding SN IIP (Grasberg et al. 1971; Chevalier 1981); a similar thin shell with small mass ($\sim 10^{-6} M_\odot$) is present in the hydrodynamic model of SN 2020jfo (Utrobin & Chugai 2024). Three hours later after the SBO, the interaction with the wind increases the thin shell mass up to $\sim 10^{-5} M_\odot$, while the shell density contrast with respect to the preshock wind amounts to $\sim 10^4$. The heavy deceleration of the thin shell suggests the significant effective acceleration $g = -d^2 R/dt^2 \sim 2 \times 10^3 \text{ cm s}^{-2}$, while the high density contrast ($\rho_2/\rho_1 \sim 10^4$) implies the large Atwood number $A = (\rho_2 - \rho_1)/(\rho_1 + \rho_2) \sim 10^4$. The large g and A result in the exponential growth of the RT instability with the increment $\gamma \approx \sqrt{Agk} \sim 3 \times 10^{-3}/\lambda_{13} \text{ s}^{-1}$, where $\lambda = 2\pi/k$ and λ_{13} is in

units of 10^{13} cm.

Perturbations in the form of spikes of dense gas penetrate the hot rarefied gas; the latter, in turn, forms bubbles that decelerate the dense shell between spikes. In the non-linear stage the exponential growth is replaced by the spike growth as $h \approx Agt^2$ (Fermi & von Neumann 1953). In fact, the spike growth is limited by the KH instability that results in the spike stripping and the formation of mushroom structures which are apparent in 3D numerical simulations (e.g., Blondin & Ellison 2001). As a result, the KN instability brings about an ensemble of corrugated sheets of dense line-emitting fragments embedded in the rarefied hot gas of the forward shock. The collateral turbulence results in the progressive fragmentation and mixing of fragments. Eventually, dense fragments dissolve and the broad He II 4686 Å emission disappears. This scenario permits us to understand the early emergence and a brief lifetime of the broad He II 4686 Å emission.

An interesting outcome of the proposed model for the early broad emission of the He II 4686 Å line is an expected flash of a broad emission of the O VI 1032, 1038 Å resonance doublet coeval with the fading 4686 Å line. The point is that the advanced fragmentation results in the increase of fragments total surface area, which brings about a more efficient heating that would favor the high emissivity of the O VI resonant doublet at the temperature of $\sim 10^5$ K. The predicted O VI 1032, 1038 Å emission would have the same width as the broad 4686 Å line, in contrast to lines with narrow core and broad wings originating from the photoionized preshock wind (Groh 2014).

5 CONCLUSIONS

Below is a brief résumé of major results.

- We propose the model of the broad He II 4686 Å emission in the early spectrum of SN 2020jfo and the scenario that accounts for the early emergence and a brief duration of this emission.
- The broad 4686 Å line is emitted by fragments of the boundary thin dense shell embedded in a hot gas of the adiabatic forward shock. The shell fragmentation and the subsequent fragments mixing with hot gas is the outcome of the RT instability.
- Calculations of the ionization and excitation of helium and hydrogen reproduce the He II 4686 Å luminosity, the large flux ratio 4686 Å/ $H\alpha$, and a significant optical depth of the 4686 Å line.
- It is shown that the fragment heating can be produced by hot electrons of the forward shock.

6 REFERENCES

- Andrews J. E., Sand D. J., Valenti S. et al., *Astrophys. J.* **885**, 43 (2019)
- Blinnikov S. I., AIP Conference Proceedings **1016**, 241 (2008)
- Blinnikov S. I., Bartunov O. S., *Astron. Astrophys.* **273**, 106 (1993)
- Blondin J. M., Ellison D. C., *Astrophys. J.* **560**, 244 (2001)
- Bohigas J., *Astrophys. J.* **674**, 954 (2022)
- Breizman B. N., Aleynikov P., Hollmann E. M., Lehnen M., *Nuclear Fusion* **59**, Issue 8, article id. 083001 (2019)
- Bullivant C. et al., *Monthly Not. R. Astron. Soc.* **476**, 1497 (2018)
- Chevalier R. A., Fransson C., Nymark T. K., *Astrophys. J.* **641**, 1029 (2006)
- Chevalier R. A., *Astrophys. J.* **258**, 790 (1982a)
- Chevalier R. A., *Astrophys. J.* **259**, 302 (1982b)
- Chevalier R. A., *Fundamentals Cosmic Phys.*, **7**, 1 (1981)
- Chugai N. N., *Monthly Not. R. Astron. Soc.* **494**, L86 (2020)
- Chugai N. N., Blinnikov S. I., Fassia A. et al., *Monthly Not. R. Astron. Soc.* **330**, 473 (2002)
- Chugai N. N., *Monthly Not. R. Astron. Soc.* **326**, 1448 (2001)
- Dessart L., Hillier D. J., Audit E., *Astron. Astrophys.* **603A**, 51 (2017)
- Fermi E., von Neumann J., Technical Report no. AECU-2979, Los Alamos Scientific Laboratory, (OSTI ID: 4373391) (1953)
- Grasberg E. K., Imshennik V. S., Nadyozhin D. K., *Astrophys. Space Sci.* **10**, 3 (1971)
- Grefenstette B. W., Brightman M., Earnshaw H. P., Harrison F. A., Margutti R., *Astrophys. J.* **952**, id. L3, 6 pp. (2023)
- Groh J. H., *Astron. Astrophys.* **572**, L11 (2014)
- Jacobson-Galán W. V., Dessart L., Margutti R. et al., *Astrophys. J.* **954**, L42 (2023)
- Morozova V., Piro A. L., Valenti S, *Astrophys. J.* **838**, 28 (2017)
- Nadyozhin D. K., *Astrophys. Spce Sci.* **112**, 225 (1985)
- Osterbrock D. E., Ferland G. J., *Astrophysics of gaseous nebulae and active galactic nuclei* USA: University Science Books, 2006
- Quimby R. M., Wheeler J. C., Höflich P. et al., *Astrophys. J.* **666**, 1093 (2007)
- Shrestha M., Pearson J., Wyatt S. et al., eprint arXiv:2310.00162 (2023)
- Teja R. S., Singh A., Sahu D. K. et al., *Astrophys. J.* **930**, 34 (2022)

- Utrobin V. P., Chugai N. N., Monthly Not. R. Astron. Soc. **527**, 6227 (2024)
- Vernazza J. E., Avrett E. H., Loeser R., Astrophys. J. Suppl. Ser. **45**, 635 (1981)
- van Regemorter H., Astrophys. J. **136**, 906 (1962)
- Yadav N., Ray A., Chakraborti S. et al., Astrophys. J. **782**, 30 (2014)
- Yaron O., Perley D. A., Gal-Yam A. et al., Nature Physics **13**, 510 (2017)